ChemComm

COMMUNICATION

View Article Online
View Journal | View Issue

Cite this: *Chem. Commun.*, 2023, 59, 7982

Received 23rd March 2023,
Accepted 30th May 2023

DOI: 10.1039/d3cc01437a

rsc.li/chemcomm

Localised degradation within sulfide-based all-solid-state electrodes visualised by Raman mapping†

Jungwoo Lim, [ab] Yundong Zhou,‡[ab] Rory H. Powell,[ab] Tugce Ates,[cd] Stefano Passerini [cde] and Laurence J. Hardwick *[ab]

The distribution of degradation products, before and after cycling, within common sulfide-based solid electrolytes (β-Li_3PS_4, Li_6PS_5Cl and $Li_{10}GeP_2S_{12}$) was mapped using Raman microscopy. All composite electrodes displayed the appearance of side reaction products after the initial charge-discharge cycle, located at the site of a $LiNi_{0.6}Mn_{0.2}Co_{0.2}O_2$ particle.

The development of sulfide-based lithium superionic conductors ($>10^{-4}$ S cm^{-1}) has addressed the challenge of low ionic conductivity, spurring the development of all-solid-state batteries (ASSB).[1,2] Despite the suitable ionic conductivity of sulfide-based materials, they can be challenging to handle due to interfacial instability against active materials (electrodes and conductive binder) within the cell. The limited electrochemical window of sulfide solid electrolytes (of *ca.* 2–3 V *vs.* Li/Li^+) can trigger chemical and electrochemical decomposition within the cell that leads to limited cell life.[3] Previously, solid electrolyte decomposition has been analysed *ex situ* from recovered pellets or powders after reaction by X-ray photoelectron spectroscopy, powder X-ray diffraction and time-of-flight secondary ion mass spectrometry.[4–6] Furthermore, Raman microscopy has been widely used for analysing ASSB electrodes, both *in situ* and *ex situ*, due to the ability to spatially map the chemical composition down to micron scale resolution. Raman mapping enables facile analysis, as well as direct chemical visualisation of the evolution of interfaces within practical electrode composites, after or during electrochemical treatment.[7–9]

To study the interfacial behaviour within more representative cell types, the scalable method of tape-casting (wet slurry fabrication) was adopted for electrode stack preparation[10,11] and analysed by *ex situ* Raman microscopy. Previously, Raman spectroscopy has been used to map the charge heterogeneity of positive electrodes[7] and *in situ* Raman analysis has highlighted the decomposition behaviour of Li_6PS_5Cl at the interface of both $LiCoO_2$ and lithium metal.[9]

$LiNi_{0.6}Mn_{0.2}Co_{0.2}O_2$ was charged and discharged against lithium metal using one of three sulfide-based solid electrolytes (β-Li_3PS_4, Li_6PS_5Cl or $Li_{10}GeP_2S_{12}$) from 3 to 4.2 V (*vs.* Li/Li^+). Charging capacity among the cells showed slight variation between them: 159 mA h g^{-1} for β-Li_3PS_4, 172 mA h g^{-1} for Li_6PS_5Cl and 183 mA h g^{-1} for $Li_{10}GeP_2S_{12}$ (Fig. 1). The

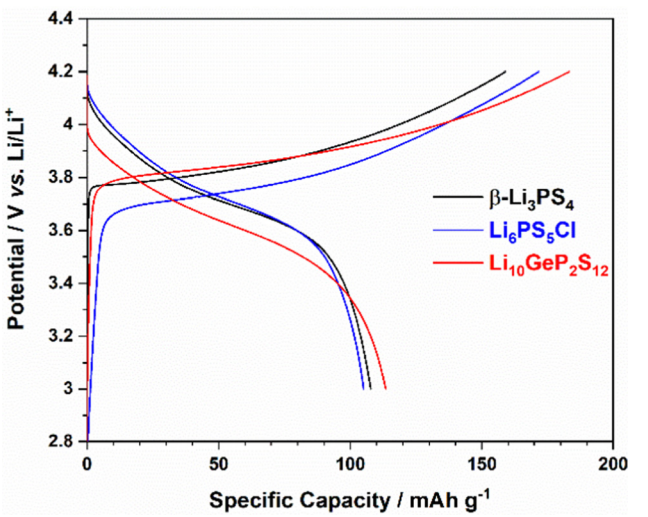

Fig. 1 First charge/discharge profile of $LiNi_{0.6}Mn_{0.2}Co_{0.2}O_2$ cycled between 3.0 V and 4.2 V *vs.* Li/Li^+, comprising either β-Li_3PS_4, Li_6PS_5Cl or $Li_{10}GeP_2S_{12}$ as the solid electrolyte.

[a] *Stephenson Institute for Renewable Energy, Department of Chemistry, University of Liverpool, Liverpool L69 7ZF, UK. E-mail: hardwick@liverpool.ac.uk*
[b] *The Faraday Institution, Harwell Campus, Didcot, OX11 0RA, UK*
[c] *Helmholtz Institute Ulm (HIU), Helmholtzstrasse 11, Ulm 89081, Germany*
[d] *Karlsruhe Institute of Technology (KIT), P.O. Box 3640, Karlsruhe 76021, Germany*
[e] *Chemistry Department, Sapienza University of Rome, Piazzale A. Moro 5, Rome 00185, Italy*

† Electronic supplementary information (ESI) available. See DOI: https://doi.org/10.1039/d3cc01437a

‡ Present address: National Physical Laboratory, Hampton Rd, Teddington, TW11 0LW, UK.

variability derives from small differences in ionic conductivities and contact resistances between the three studied solid electrolytes and the active material $LiNi_{0.6}Mn_{0.2}Co_{0.2}O_2$. $Li_{10}GeP_2S_{12}$ has the highest reported ionic conductivity amongst the three-sulfide solid electrolytes investigated ($\sim 10^{-2}$ S cm^{-1}) and showed almost similar charging capacity (when charged to 4.2 V limit) compared to $LiNi_{0.6}Mn_{0.2}Co_{0.2}O_2$ within a conventional liquid carbonate electrolyte (Fig. S1, ESI†).[12,28] For the discharge, although each electrode has varying voltage hysteresis, all electrodes show a comparable discharge capacity of around 110 mA h g^{-1} (compared to 160 mA h g^{-1} within a liquid electrolyte, Fig. S1, ESI†).

Considering the narrow electrochemical window of all sulfide solid electrolytes,[3,4] the interfacial decomposition between solid electrolytes and the active material account for some of the irreversible capacity within the 1st cycle. Since the decomposition of solid electrolytes forms various insulating side products, Raman microscopy was used to identify the chemical nature and type of these products before and after electrochemical cycling.

Raman spectra from all components ($LiNi_{0.6}Mn_{0.2}Co_{0.2}O_2$; conductive additive: vapour grown carbon fibres (VGCF); binder: polyisobutene; solid electrolyte – Fig. S3 and S4, ESI†) of the positive solid-state electrode were collected. Peak assignments are listed within Table 1 and used for the generation of chemical distribution maps. All the samples are recovered and measured under an inert argon atmosphere to avoid air contamination.

Fig. 2 shows typical pristine and cycled spectra for each of the three solid electrolytes containing composite electrodes (refer to Section 1.2 in the ESI† for the composition). Although bands from $LiNi_{0.6}Mn_{0.2}Co_{0.2}O_2$ and sulfide solid electrolytes overlap in the 400–700 cm^{-1} region, all pristine electrodes show a clearly distinguishable peak at 420 cm^{-1} ascribed to $(PS_4)^{3-}$ from the sulfide solid electrolyte, distinct from the A_{1g} peak of $LiNi_{0.6}Mn_{0.2}Co_{0.2}O_2$ (597 cm^{-1}). The VGCF carbon additives have two distinctive peaks similar to graphitic carbon, the D band and the G^- and G^+ bands, which are located at *ca.* 1330 cm^{-1}, 1580 and 1610 cm^{-1} respectively.[17] In addition, uncycled Li_6PS_5Cl and $Li_{10}GeP_2S_{12}$ electrodes show a negligible amount of S_x (x = 4–8) product at 473 cm^{-1}, which is commonly observed as the chemical decomposition product between sulfide solid electrolytes and metal oxides when they are mixed together.[5] After galvanostatic testing, all the electrodes measured showed the presence of new bands, relating to the formation of decomposition products.

In all three cases the main Raman band in the solid electrolyte ($\upsilon_s(PS_4)^{3-}$) remains detectable, indicating that

Table 1 Raman peak positions and assignments of solid electrolyte compounds

Wavenumber/cm^{-1}	Assignment	Ref.
348	υ_s (GeS_2)	13 and 14
356	υ_s $(GeS_4)^{3-}$	13 and 14
380	A_{1g} from P_2S_x	9 and 15
420	υ_s $(PS_4)^{3-}$	9
473	S–S bending from S_x	9
597	A_{1g} from $LiNi_{0.6}Mn_{0.2}Co_{0.2}O_2$	16
1330	D band (VGCF)	17
1430	$\delta(CH_3)$–S	18–20
1580, 1610	G^-, G^+ band (VGCF)	17

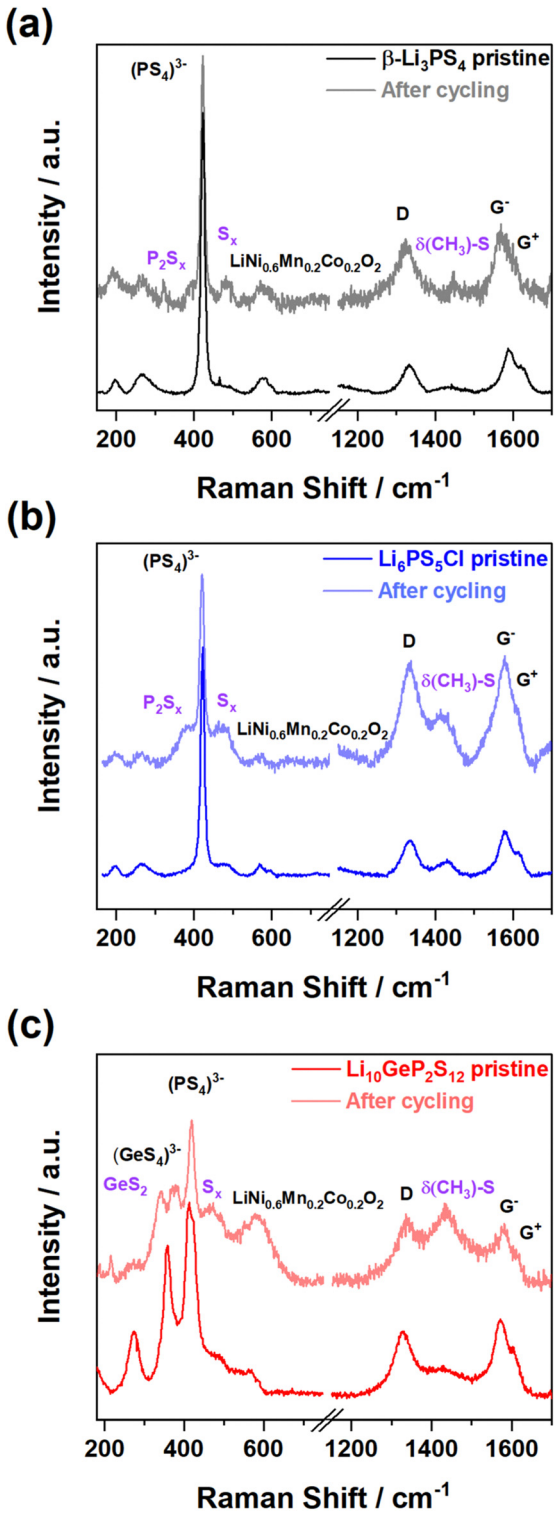

Fig. 2 Representative Raman spectra from contour mapping of uncycled and cycled composite electrodes: (a) β-Li_3PS_4, (b) Li_6PS_5Cl, and (c) $Li_{10}GeP_2S_{12}$.

decomposition is interfacial rather than a bulk degradation process. Firstly, β-Li_3PS_4 decomposed to the compounds, P_2S_x (where x is *ca.* 5) (380 cm^{-1}) and S_x (473 cm^{-1}).[9] For Li_6PS_5Cl, it initially decomposed to Li_3PS_4, before forming both P_2S_x and S_x. β-Li_3PS_4 has the $(PS_4)^{3-}$ vibration at a similar wavenumber to Li_6PS_5Cl, which can make the appearance of P_2S_x challenging to differentiate from Li_6PS_5Cl; however, S_x compounds were found from the spectra at 473 cm^{-1}.[9] For $Li_{10}GeP_2S_{12}$, Ge–S bonding decomposes into GeS_2 and S_x, found in the spectra in Fig. 2c at 348 cm^{-1} and 473 cm^{-1}.

All spectra show a broad band centred at 1430 cm^{-1}, which cannot be easily assigned by examining the spectra of the individual components (Fig. S3, ESI†). To investigate the origin of this peak, Raman spectra of various slurry mixtures were collected before and after removal of the solvent (Fig. S5 and S6, ESI†). Although slurry samples have strong fluorescence background from organic materials (binder: polyisobutene and solvent: toluene),[21] samples containing carbon have a broad 1430 cm^{-1} band, which is also observed when the dry powders are combined. This suggests that the 1430 cm^{-1} band arises from reaction of the carbon additive with the solid electrolyte during the electrode preparation. Previously, side reaction between toluene and β-Li_3PS_4 or Li_6PS_5Cl has been reported.[22,23] To determine whether this is also the case with other sulfide electrolytes, $Li_{10}GeP_2S_{12}$ was mixed within toluene, and GeS_2 (348 cm^{-1}) was detected after drying the slurry (Fig. S6, ESI†). Contributions from the binder through vulcanisation reactions or binder degradation were also considered, but these reactions require mild heating (~150 °C and/or UV irradiation)[24,25] and other observations of binder degradation generally occur after electrochemical testing.[26,27] Taking this all into account and the absence of the prominent 700 cm^{-1} band of polyisobutene in any spectra leads to the conclusion that the band appears from reaction between the electrolytes and the carbon additive. Indeed, the band at 1430 cm^{-1} has been previously reported from the reaction between few-layer graphene and S_8.[18] This peak is also present in the spectrum of methanethiol (CH_3SH) and other linear dithiols[19,20] suggesting that the bands arise from CH_3 surface functional groups and S linkers, and can be denoted as δ(CH_3)–S.

The representative contour mapping image of the β-Li_3PS_4 based pristine electrode is shown in Fig. 3 and Li_6PS_5Cl and $Li_{10}GeP_2S_{12}$ contour mappings are available in the ESI† (Fig. S7 and S9). The existence of components from each mapping point was obtained from the spectra and the intensities were normalised. Red colour on the contour scale indicates a relatively intense relevant Raman peak representing the clear presence of a specific component. Black means the absence of the relevant Raman peak above the signal to noise for a specific component at the designated area or spot. From Fig. 3, the location and distribution of $LiNi_{0.6}Mn_{0.2}Co_{0.2}O_2$ and β-Li_3PS_4 of carbon, based upon their distinctive peaks (listed in Table 1), can be observed. No significant Raman signals of decomposition products resulting from the contact of all materials with the solid electrode were observed.

Fig. 4 shows the Raman contour mapping of electrodes after electrochemical cycling. The main bands of β-Li_3PS_4 electrolyte

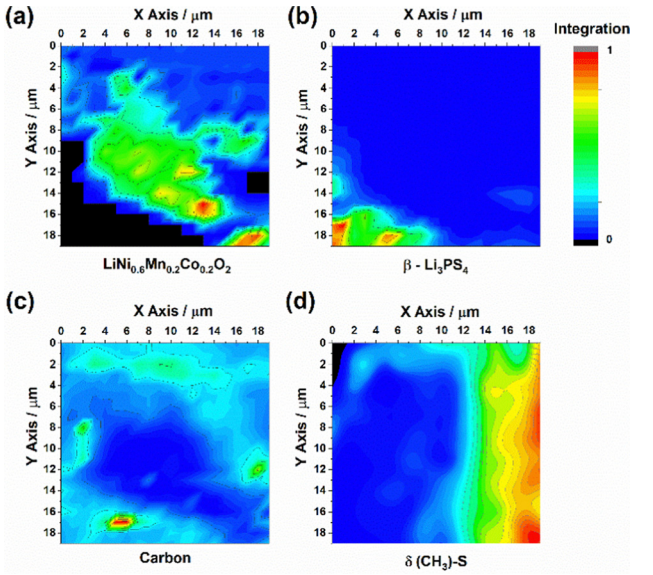

Fig. 3 Raman contour mapping image of the pristine β-Li_3PS_4 positive electrode containing active material, carbon additive (VGCF) and electrolyte. Raman contour maps of bands pertaining to (a) $LiNi_{0.6}Mn_{0.2}Co_{0.2}O_2$, (b) β-$Li_3PS_4$, (c) the carbon additive and (d) δ(CH_3)–S. Red contours represent the presence of intense bands, blue contour trace presence and black, band not detected.

do not overlap with $LiNi_{0.6}Mn_{0.2}Co_{0.2}O_2$ or the carbon bands, and thereby each component is distinguishable. Moreover, Fig. 4 shows the distribution of decomposition products of β-Li_3PS_4, P_2S_5 and S_x from the map. These decomposition products are located between $LiNi_{0.6}Mn_{0.2}Co_{0.2}O_2$ and β-Li_3PS_4, suggesting that this sulfide SE decomposition is an interfacial reaction. $Li_{10}GeP_2S_{12}$ and Li_6PS_5Cl have similar decomposition behaviour (Fig. S7–S10, ESI†). In particular, polysulfide (S_x) species were detected on both β-Li_3PS_4 and Li_6PS_5Cl solid electrolytes in the vicinity of $LiNi_{0.6}Mn_{0.2}Co_{0.2}O_2$. A similar observation was made with Raman measurements on the $LiCoO_2$ and Li_6PS_5Cl solid–solid interface,[9] highlighting the oxidative stability of the electrolyte breakdowns when in contact with partially de-lithiated positive electrode materials. Though the negative effects of carbon additives on degradation have been frequently reported,[29,30] from this initial study no correlation of the degradation products with carbon position was observed. Mapping studies, using a variety of carbons will be probed, as well as *in situ* mapping investigations to further understand the origin and location of composite electrode degradation. Moreover, to exclude any laser heating effects during electrode mapping, the laser power was minimised to 43 μW. All electrode components were also found to be stable at greater laser intensities (Fig. S11, ESI†).

In summary, Raman maps display the distribution of each component within the solid-state electrode at 1–2 micron resolution and show interfacial decomposition between the solid electrolyte and $LiNi_{0.6}Mn_{0.2}Co_{0.2}O_2$. In addition, during the electrode preparation, carbon contamination from sulfide solid electrolyte was found, forming surface δ(CH_3)–S. This result highlights the importance of choosing appropriate

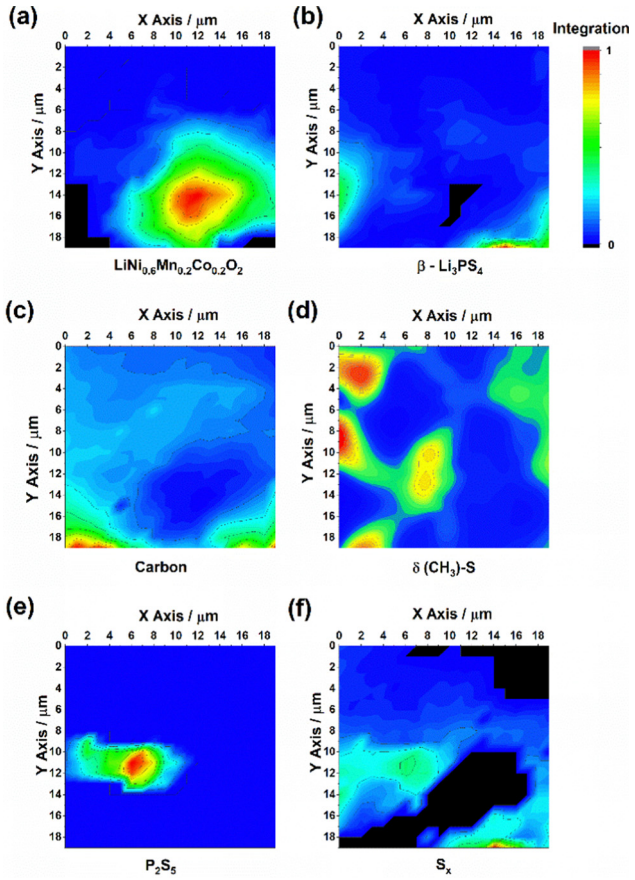

Fig. 4 Raman contour mapping images of the β-Li_3PS_4 composite electrode after electrochemical cycling. (a) $LiNi_{0.6}Mn_{0.2}Co_{0.2}O_2$, (b) β-$Li_3PS_4$, (c) carbon additive (VGCF), (d) δ(CH_3)–S, (e) P_2S_x and (f) S_x.

binder/solvent candidates and lowering the carbon amount present. Both chemical and electrochemical degradation within sulfide solid electrolytes and $LiNi_{0.6}Mn_{0.2}Co_{0.2}O_2$ produces electrically resistive side reaction products, resulting in the lowering of the cell performance, highlighting the need to suppress interfacial decomposition *via* surface protection.

The authors acknowledge the financial support from the Faraday Institution CATMAT (EP/S003053/1, FIRG016) and SOLBAT (EP/R042047/1, FIRG007) projects. T. A. and S. P. acknowledge the basic funding from the Helmholtz Association.

Conflicts of interest

There are no conflicts to declare.

Notes and references

1 L. Zhou, N. Minafra, W. G. Zeier and L. F. Nazar, *Acc. Chem. Res.*, 2021, **54**, 2717–2728.
2 M. Pasta, D. Armstrong, Z. L. Brown, J. Bu, M. R. Castell, P. Chen, A. Cocks, S. A. Corr, E. J. Cussen, E. Darnbrough, V. Deshpande, C. Doerrer, M. S. Dyer, H. El-Shinawi, N. Fleck, P. Grant, G. L. Gregory, C. Grovenor, L. J. Hardwick, J. T. S. Irvine, H. J. Lee, G. Li, E. Liberti, I. McClelland, C. Monroe, P. D. Nellist, P. R. Shearing, E. Shoko, W. Song, D. S. Jolly, C. I. Thomas, S. J. Turrell, M. Vestli, C. K. Williams, Y. Zhou and P. G. Bruce, *J. Phys. Energy*, 2020, **2**, 032008.
3 Y. Nikodimos, C.-J. Huang, B. W. Taklu, W.-N. Su and B. J. Hwang, *Energy Environ. Sci.*, 2022, **15**, 991–1033.
4 D. H. S. Tan, E. A. Wu, H. Nguyen, Z. Chen, M. A. T. Marple, J.-M. Doux, X. Wang, H. Yang, A. Banerjee and Y. S. Meng, *ACS Energy Lett.*, 2019, **4**, 2418–2427.
5 F. Walther, R. Koerver, T. Fuchs, S. Ohno, J. Sann, M. Rohnke, W. G. Zeier and J. Janek, *Chem. Mater.*, 2019, **31**, 3745–3755.
6 K. Yoon, J.-J. Kim, W. M. Seong, M. H. Lee and K. Kang, *Sci. Rep.*, 2018, **8**, 8066.
7 M. Otoyama, Y. Ito, A. Hayashi and M. Tatsumisago, *J. Power Sources*, 2016, **302**, 419–425.
8 M. Otoyama, Y. Ito, A. Sakuda, M. Tatsumisago and A. Hayashi, *Phys. Chem. Chem. Phys.*, 2020, **22**, 13271–13276.
9 Y. Zhou, C. Doerrer, J. Kasemchainan, P. G. Bruce, M. Pasta and L. J. Hardwick, *Batters. Supercaps*, 2020, **3**, 647–652.
10 T. Ates, M. Keller, J. Kulisch, T. Adermann and S. Passerini, *Energy Storage Mater.*, 2019, **17**, 204–210.
11 K. Chen, S. Shinjo, A. Sakuda, K. Yamamoto, T. Uchiyama, K. Kuratani, T. Takeuchi, Y. Orikasa, A. Hayashi, M. Tatsumisago, Y. Kimura, T. Nakamura, K. Amezawa and Y. Uchimoto, *J. Phys. Chem. C*, 2019, **123**, 3292–3298.
12 A. Choi, J. Lim, H.-J. Kim, S. C. Jung, H.-W. Lim, H. Kim, M.-S. Kwon, Y. K. Han, S. M. Oh and K. T. Lee, *Adv. Energy Mater.*, 2018, **8**, 1702514.
13 Y. Sun, W. Yan, L. An, B. Wu, K. Zhong and R. Yang, *Solid State Ion.*, 2017, **301**, 59–63.
14 I. Seo and S. W. Martin, *Inorg. Chem.*, 2011, **50**, 2143–2150.
15 Q. Pang, X. Liang, A. Shyamsunder and L. F. Nazar, *Joule*, 2017, **1**, 871–886.
16 E. Flores, P. Novák and E. J. Berg, *Front. Energy Res.*, 2018, **6**, DOI: 10.3389/fenrg.2018.00082.
17 P. W. Ruch, L. J. Hardwick, M. Hahn, A. Foelske, R. Kötz and A. Wokaun, *Carbon*, 2009, **47**, 38–52.
18 C. Bautista-Flores, J. S. Arellano-Peraza, R. Y. Sato-Berrú, E. Camps and D. Mendoza, *Chem. Phys. Lett.*, 2016, **665**, 121–126.
19 I. W. May and E. L. Pace, *Spectrochim. Acta, Part A*, 1968, **24**, 1605–1615.
20 J. Kubackova, I. Izquierdo-Lorenzo, D. Jancura, P. Miskovsky and S. Sánchez-Cortés, *Phys. Chem. Chem. Phys.*, 2014, **16**, 11461–11470.
21 L. Cabo-Fernandez, A. R. Neale, F. Braga, I. V. Sazanovich, R. Kostecki and L. J. Hardwick, *Phys. Chem. Chem. Phys.*, 2019, **21**, 23833–23842.
22 K. Lee, S. Kim, J. Park, S. H. Park, A. Coskun, D. S. Jung, W. Cho and J. W. Choi, *J. Electrochem. Soc.*, 2017, **164**, A2075.
23 J. Ruhl, L. M. Riegger, M. Ghidiu and W. G. Zeier, *Adv. Energy Sustainability Res.*, 2021, **2**, 2000077.
24 K. Lee, J. Lee, S. Choi, K. Char and J. W. Choi, *ACS Energy Lett.*, 2019, **4**, 94–101.
25 T. Y. Kwon, K. T. Kim, D. Y. Oh, Y. B. Song, S. Jun and Y. S. Jung, *Energy Storage Mater.*, 2022, **49**, 219–226.
26 R. Black, S. H. Oh, J.-H. Lee, T. Yim, B. Adams and L. F. Nazar, *J. Am. Chem. Soc.*, 2012, **134**, 2902–2905.
27 J. Lim, A. Choi, H. Kim, S. W. Doo, Y. Park and K. T. Lee, *J. Power Sources*, 2019, **426**, 162–168.
28 A. Choi, J. Lim, H. Kim, S. W. Doo and K. T. Lee, *ACS Appl. Energy Mater.*, 2019, **2**, 3427–3434.
29 F. Walther, S. Randau, Y. Schneider, J. Sann, M. Rohnke, F. H. Richter, W. G. Zeier and J. Janek, *Chem. Mater.*, 2020, **32**(14), 6123–6136.
30 E. Quemin, R. Dugas, T. Koç, B. Hennequart, R. Chometon and J.-M. Tarascon, *ACS Appl. Mater. Interfaces*, 2022, **14**(43), 49284–49294.